Front. Phys.
https://doi.org/10.15302/frontphys.2026.085208
CN 11-5994/O4
ISSN 2095-0462

RESEARCH ARTICLE

Dense arrays of aligned quasi-1D Bi_4Br_4 topological insulator nanoribbons achieved via lattice-guided oriented epitaxy on WTe_2

Shiqi Xu[1,2], Xu Zhang[1,2], Liu Yang[1,2], Yina Dong[1,2], Shuo Qi[1], Jiangyue Bai[1,2], Haizhen Gao[1,2], Nan Cheng[1,2], Yu Zhou[1,2], Liyuan Zhao[3], Limei Cha[4], Dongfei Wang[1], Zhiwei Wang[1,2], Junfeng Han[1,2,‡]

[1] Centre for Quantum Physics, Key Laboratory of Advanced Optoelectronic Quantum Architecture and Measurement (MOE), School of Physics, Beijing Institute of Technology, Beijing 100081, China
[2] International Center for Quantum Materials, Beijing Institute of Technology, Zhuhai 519000, China
[3] Experimental Center for Advanced Materials, School of Materials Science and Engineering, Beijing Institute of Technology, Beijing 100081, China
[d] Program of Materials Science and Engineer, Guangdong Technion Israel Institute of Technology, Shantou 515063, China
Corresponding authors. E-mail: ‡pkuhjf@bit.edu.cn
Received January 28, 2026; accepted June 2, 2026

Abstract

Bi_4Br_4, an emerging quasi-1D topological insulator, exhibits rich topological phases and great potential for low-power electronics and topological quantum computing. High-quality, oriented Bi_4Br_4 films are essential for exploring low-dimensional topological physics and developing functional devices. However, the growth of such films is highly challenging due to their sensitivity to growth parameters, and current synthesis techniques can only yield randomly oriented or multidirectional Bi_4Br_4 nanostructures, which impedes the study of intrinsic anisotropy and device integration. Here, we demonstrate a molecular beam epitaxy approach using anisotropic WTe_2 as an epitaxial template to achieve oriented Bi_4Br_4 nanoribbon arrays with controlled thickness. Through systematic optimization of growth temperature, source rate ratio and annealing conditions, we established the optimal window for high-quality nanoribbon synthesis. The resulting nanostructures exhibit well-defined morphologies and sharp edges, with a thickness of 2–9 nm. This work establishes a viable route for the oriented growth of Bi_4Br_4 and provides an ideal platform for investigating topological edge transport, anisotropic phenomena, and the design of topological quantum devices.

Keywords oriented growth, Bi_4Br_4 nanoribbons, quasi-1D topological insulator, WTe_2, molecular beam epitaxy, van der Waals heterostructures

Just Accepted

This is a “Just Accepted” manuscript, which has been examined by the peer-review process and has been accepted for publication. A “Just Accepted” manuscript is published online shortly after its acceptance, which is prior to technical editing and formatting and author proofing. Higher Education Press (HEP) provides “Just Accepted” as an optional and free service which allows authors to make their results available to the research community as soon as possible after acceptance. After a manuscript has been technically edited and formatted, it will be removed from the “Just Accepted” Web site and published as an Online First article. Please note that

RESEARCH ARTICLE

Dense arrays of aligned quasi-1D Bi_4Br_4 topological insulator nanoribbons achieved via lattice-guided oriented epitaxy on WTe_2

Shiqi Xu[1,2], Xu Zhang[1,2], Liu Yang[1,2], Yina Dong[1,2], Shuo Qi[1], Jiangyue Bai[1,2], Haizhen Gao[1,2], Nan Cheng[1,2], Yu Zhou[1,2], Liyuan Zhao[3], Limei Cha[4], Dongfei Wang[1], Zhiwei Wang[1,2], Junfeng Han[1,2,‡]

[1] Centre for Quantum Physics, Key Laboratory of Advanced Optoelectronic Quantum Architecture and Measurement (MOE), School of Physics, Beijing Institute of Technology, Beijing 100081, China
[2] International Center for Quantum Materials, Beijing Institute of Technology, Zhuhai 519000, China
[3] Experimental Center for Advanced Materials, School of Materials Science and Engineering, Beijing Institute of Technology, Beijing 100081, China
[d] Program of Materials Science and Engineer, Guangdong Technion Israel Institute of Technology, Shantou 515063, China
Corresponding authors. E-mail: ‡pkuhjf@bit.edu.cn
Received January 28, 2026; accepted June 2, 2026

Abstract

Bi_4Br_4, an emerging quasi-1D topological insulator, exhibits rich topological phases and great potential for low-power electronics and topological quantum computing. High-quality, oriented Bi_4Br_4 films are essential for exploring low-dimensional topological physics and developing functional devices. However, the growth of such films is highly challenging due to their sensitivity to growth parameters, and current synthesis techniques can only yield randomly oriented or multidirectional Bi_4Br_4 nanostructures, which impedes the study of intrinsic anisotropy and device integration. Here, we demonstrate a molecular beam epitaxy approach using anisotropic WTe_2 as an epitaxial template to achieve oriented Bi_4Br_4 nanoribbon arrays with controlled thickness. Through systematic optimization of growth temperature, source rate ratio and annealing conditions, we established the optimal window for high-quality nanoribbon synthesis. The resulting nanostructures exhibit well-defined morphologies and sharp edges, with a thickness of 2–9 nm. This work establishes a viable route for the oriented growth of Bi_4Br_4 and provides an ideal platform for investigating topological edge transport, anisotropic phenomena, and the design of topological quantum devices.

Keywords oriented growth, Bi_4Br_4 nanoribbons, quasi-1D topological insulator, WTe_2, molecular beam epitaxy, van der Waals heterostructures

1 Introduction

In recent years, topological materials [1-6] have emerged as a research frontier due to their unique electronic structures and potential applications in novel nanoelectronic devices [7-11]. Among diverse topological materials, bismuth halides Bi_4X_4 (X = Br, I) exhibit their rich topological phases [12-17] and diverse physical properties [18-22]. Theoretical and experimental studies confirm monolayer Bi_4Br_4 is a quantum spin Hall insulator possessing a large bandgap (~0.2 eV) [23-26], while multilayers allow multi-channel transport via weak interlayer coupling [27, 28]. Notably, bulk crystals display phase-dependent topology [12, 13, 26, 29, 30]: the α-phase is a higher-order topological insulator with topologically protected hinge states [26, 31-34], while the β-phase is a weak topological insulator [26, 35-38], together providing a versatile platform for exploring low-dimensional topological quantum effects [33, 39-43]. Structurally, Bi_4X_4 consists of van der Waals-assembled one-dimensional (1D) molecular chains [26, 29, 44, 45], forming a chain-like crystal architecture with pronounced anisotropy [19, 22, 33, 41], exhibiting distinctly different physical properties along the chain (*b*-axis) versus perpendicular directions.

A key feature of this material is its topologically protected 1D edge states [24, 28, 31, 32, 46], which enable dissipationless transport [33, 41, 43, 47, 48], and the pronounced electron confinement in its quasi-1D structure further provides an ideal platform for investigating strong correlation phenomena like Luttinger liquid behavior [49, 50]. However, current research relies primarily on bulk crystals and mechanical exfoliation. The inherent quasi-1D chain-like structure typically yields flakes with limited lateral dimensions [22, 33], making it difficult to obtain large-area thin layers. On the other hand, existing direct synthesis methods generally suffer from the problem of producing nanostructures with disordered [51] or multi-directional orientations [24, 52, 53], making the growth of well-aligned arrays a persistent challenge in the field. These limitations prohibit systematic studies of intrinsic anisotropic

properties and device integration of topological edge states. To bridge this gap, it is essential to develop directed synthesis techniques for producing aligned, atomically precise "quantum wires." Such controlled architectures would enable high-performance interconnects in integrated circuits [54, 55], reducing resistive heating and energy loss. Moreover, they represent a critical prerequisite for coupling nanowires to superconducting electrodes in Majorana-based quantum computing hardware [56, 57].

In this work, WTe_2 is selected as an epitaxial substrate to achieve oriented growth of Bi_4Br_4 nanoribbons. The anisotropic surface of Td-phase WTe_2 effectively guides 1D Bi_4Br_4 to align along specific crystallographic directions, overcoming the random orientation typical of previous methods. Through synergistic optimization of key parameters including growth temperature, source rate ratio and annealing process, we established the optimal growth window for high-quality nanoribbons. The as-prepared nanoribbons possess well-defined morphology, sharp edges, uniform *b*-axis alignment and thickness continuously tunable from 2 to 9 nm (≈ 2–9 layers). The oriented Bi_4Br_4 not only provide a unique system for exploring anisotropic physics and correlated topological effects in the 1D limit but also establishes a critical material foundation for constructing functional devices.

2 Experiential section

2.1 Sample preparation and growth procedure

The WTe_2 substrate was mounted onto a tantalum plate using silver conductive paste (EPO-TEK H20E, USA), and the assembly was secured onto a flag-style sample holder via spot-welded Ta wires, see Figure S1 in the Supporting Information (SI). To obtain an atomically flat and clean surface, the WTe_2 substrate was mechanically exfoliated using 3M Scotch tape, effectively removing surface oxides and adsorbed contaminants. The exfoliated sample was promptly transferred into the load-lock chamber. After reaching a base pressure of 5×10^{-5} Pa, it was transferred to the MBE growth chamber, where the base pressure was maintained at approximately 1×10^{-7} Pa. The substrate was subsequently annealed at 200 ℃ for 2 hours under ultra-high vacuum to further desorb residual surface adsorbates, creating an ideal interface for subsequent high-quality van der Waals epitaxy.

Following substrate pretreatment, we set the system to the target growth temperature to commence thin-film deposition. High-purity Bi (99.999%) and $BiBr_3$ (99.9%) were loaded into separate high-temperature effusion cells, allowing independent control of their deposition rates through temperature regulation. During deposition, the Bi deposition rate was monitored in real-time using a quartz crystal monitor. The rate was first stabilized at 0.25 BL min^{-1}, with 1 BL corresponding to the single-step height of Bi (111) [58]. The shutter was then opened to begin deposition, and the process duration was varied from 5 to 30 minutes depending on the desired thickness. Subsequently, the pre-deposited Bi layer was annealed at the same temperature, followed by exposure to $BiBr_3$ vapor. This step enabled the reaction between Bi and $BiBr_3$ to form stoichiometrically controlled Bi_4Br_4 thin films, ultimately yielding a Bi_4Br_4/WTe_2 van der Waals heterostructure.

2.2 Materials characterization

The structural and chemical properties of the synthesized materials were characterized using a suite of analytical techniques. Surface morphology and structural features were examined by atomic force microscopy (AFM) on a Bruker Multimode 8 system and a Bruker Dimension XR system. Elemental composition and chemical states were analyzed by X-ray photoelectron spectroscopy (XPS) using a PHI QUANTERA-II SXM instrument with a monochromatic Al Kα X-ray source (1486.6 eV). Crystal structure was assessed via X-ray diffraction (XRD) on a Bruker D2 Phaser diffractometer with Cu-Kα radiation (λ = 1.54184 Å). Quantitative elemental analysis was performed using a JEOL JSM-IT700HR scanning electron microscope (SEM) equipped with an energy-dispersive X-ray spectroscopy (EDS) detector. Raman spectroscopy measurements were conducted on a WITec alpha 300 system with a 532 nm laser source and a 50× objective to probe lattice vibrational modes. The lattice structure of the nanoribbons and their epitaxial relationship with the WTe_2 substrate were characterized by scanning tunneling microscopy (STM, CreaTec LT-STM system) and transmission electron microscopy (TEM, Thermo Scientific Talos F200X system). Cross-sectional lamellae for TEM observation were prepared using a focused ion beam (FIB, Thermo Scientific Helios 5 UC system).

3 Results and discussion

Bismuth bromide (Bi_4Br_4), a member of the bismuth halide Bi_4X_4 family, has recently emerged as a promising topological quantum material [13, 25, 31-33, 43], attracting broad interest due to its distinctive electronic structure and potential applications. Bulk Bi_4Br_4 crystallizes in a monoclinic structure with the space group C2/m [32]. The

unit cell consists of 1D molecular chains extending along the *b*-axis, which align parallel along the *a*-direction, with each layer containing two such chains (Figure 1a). The stacking sequence between layers determines the polytype; to date, only the α-phase has been experimentally confirmed in bulk crystals [13]. In this phase, layers adopt an AB stacking sequence along the *c*-axis, accompanied by a half-unit-cell shift along the *b*-axis and a 180° rotation between adjacent layers [29]. Within each chain, Bi atoms form a zigzag backbone via strong covalent bonding, while Br atoms terminally bond to outer Bi sites, forming near-vertical configurations with bond angles $\alpha \approx 91°$ and $\beta \approx 92°$. The corresponding lattice parameters are a = 13.064 Å, b = 4.338 Å, and c = 20.061 Å [13]. The pronounced contrast between strong intrachain covalent bonds and weak interchain/interlayer van der Waals interactions facilitates cleavage along the *b*-axis or the epitaxial growth of high-quality nanoribbons without dangling bonds [13, 24, 59], making Bi_4Br_4 an ideal system for constructing topologically robust 1D electronic channels.

Structurally analogous, tungsten ditelluride (WTe_2) also exhibits strongly anisotropic quasi-1D character. As a representative layered transition metal dichalcogenide (TMDC), it adopts a thermodynamically stable orthorhombic Td phase (space group $Pnm2_1$, No. 31) under ambient conditions [60]. Its structure can be viewed as a strongly distorted variant of the ideal 1T phase, composed of distorted Te–W–Te sandwich layers stacked along the *c*-axis via van der Waals interactions (Figure 1a). Unlike high-symmetry 2H-phase TMDCs, both W and Te atoms in WTe_2 undergo dimerization displacements, forming 1D zigzag chains along the *a*-axis and leading to marked structural anisotropy. The lattice constants are a = 3.483 Å, b = 6.278 Å, and c = 14.054 Å. This low-symmetry structure breaks inversion symmetry, which is considered the structural origin of its extraordinary properties [61], such as extremely large unsaturated magnetoresistance [62] and type-II Weyl semimetal states [63]. It is noteworthy that both WTe_2 and Bi_4Br_4 exhibit strong uniaxial anisotropy along their respective axes (WTe_2: *a*-axis; Bi_4Br_4: *b*-axis). This structural commonality makes WTe_2 an ideal substrate for guiding the oriented epitaxial growth of Bi_4Br_4. Thus, such a TMDC–topological insulator van der Waals heterostructure provides a distinct platform to explore novel interfacial quantum effects [64, 65], such as charge transfer or enhanced spin–orbit coupling.

Here, we demonstrate the oriented epitaxy of Bi_4Br_4 nanoribbons on WTe_2 substrates using molecular beam epitaxy (MBE). AFM (Figure 1b) reveals that the nanoribbons with regular shapes and sharp edges extend along their intrinsic *b*-axis, aligning strictly parallel to the *a*-axis of the WTe_2 substrate, demonstrating excellent epitaxial orientation uniformity. Cross-sectional HRTEM, cut perpendicular to the nanoribbon long axis, further confirms this epitaxial relationship (Figure S2): the WTe_2 atomic arrangement corresponds to its bc-plane, showing that the nanoribbons grow oriented along the substrate's *a*-axis. Moreover, a sharp and well-defined interface is observed, where lattice fringes on both sides terminate at the interface rather than continuing across it, directly evidencing van der Waals epitaxy. Severe lattice damage and thermal decomposition induced by FIB thermal effects rendered the nanoribbon's intrinsic atomic-resolution features unobservable. HRTEM-EDS mapping (Figure S3) reveals Bi/Br in the upper film and W/Te in the underlying substrate. Unlike uniform Bi, Br is scarce and more diffuse due to heat-induced Bi–Br bond breaking and Br volatilization during FIB preparation.

These nanoribbons have an average width of ~15 nm and lengths predominantly in the 70–130 nm range. Cross-sectional height analysis (Figure 1c, along the red line in the inset) reveals a height distribution of 5–6 nm. Given that the monolayer thickness of α-Bi_4Br_4 is ~0.96 nm [25, 33], this height corresponds to stacks of approximately 5–6 molecular layers. Importantly, in multilayer Bi_4Br_4, weak interlayer coupling facilitates topological edge state decoupling at the terraced edges formed during layer-island growth and maintains independent boundary states across different layers [27], thereby offering an ideal platform for multi-channel, low-dissipation electronic transport.

To further confirm the chemical composition and bonding states of the nanoribbons, XPS analysis was performed. The survey scan (Figure 1d) shows characteristic signals originating only from the substrate (W, Te) and the target film (Bi, Br), apart from the C 1s and O 1s peaks attributed to ambient exposure. No other impurity elements were detected, indicating high chemical purity of the sample. High-resolution XPS spectra of the Bi 4f and Br 3d regions are presented in Figures 1e and 1f, respectively, providing further insight into the chemical environment. In the Bi 4f region (Figure 1e), a doublet appears at 157.4 eV and 162.7 eV, corresponding to the $4f_{7/2}$ and $4f_{5/2}$ levels in a Bi–Bi bonding configuration. Another doublet observed at higher binding energies of 159.4 eV and 164.8 eV is assigned to the corresponding orbitals in a Bi–Br bonding environment. Simultaneously, the Br 3d spectrum (Figure 1f) exhibits a well-defined doublet at 68.7 eV ($3d_{5/2}$) and 69.7 eV ($3d_{3/2}$), further confirming the formation of Br–Bi covalent bonds. All observed binding energies are in excellent agreement with literature values for Bi_4Br_4 [24, 52]. Semi-quantitative XPS analysis (shown in Table 1 in the SI) gives a Bi:Br atomic ratio of 20.09:26.31, which is close to the 1:1 stoichiometry of Bi_4Br_4, supporting the successful preparation of high-purity quasi-1D Bi_4Br_4 nanoribbons.

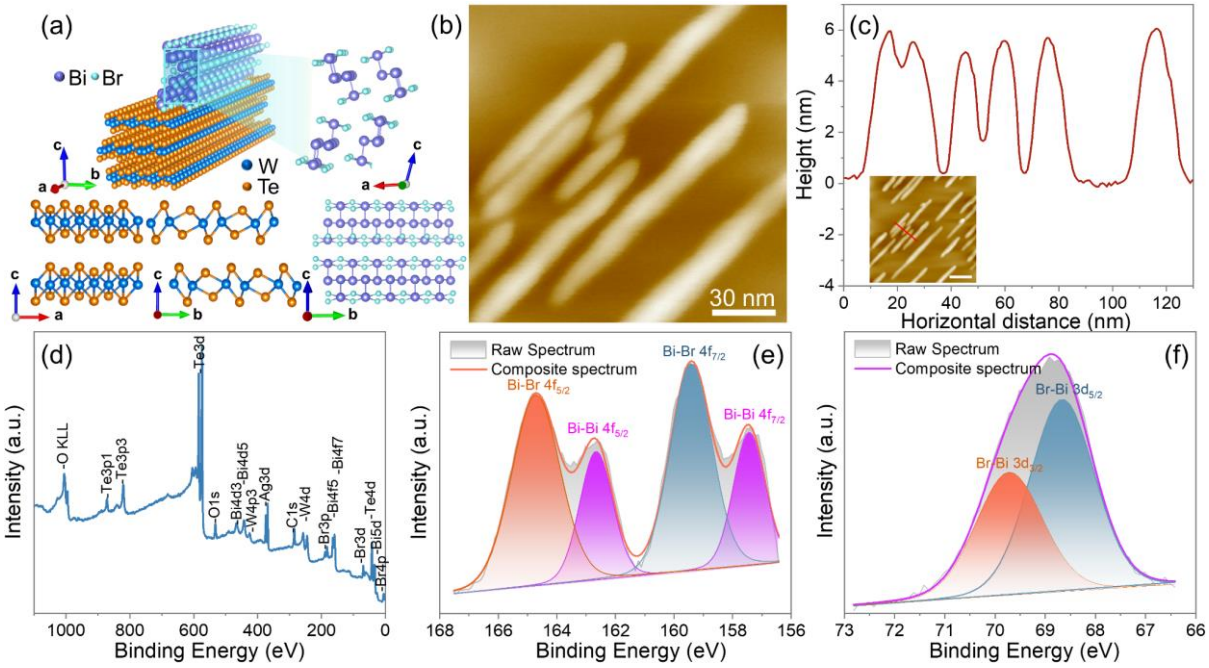

Figure 1. (a) Schematic of Bi_4Br_4/WTe_2 van der Waals heterostructure. Top-left: WTe_2 along its *a*-axis, Bi_4Br_4 along its *b*-axis, with Bi_4Br_4 growth guided by the WTe_2 *a*-axis. Bottom two panels: Te-W-Te sandwich structure of WTe_2; W and Te atoms undergo dimerization displacements, forming 1D zigzag chains along the *a*-axis and van der Waals layered stacking along the *c*-axis. Right panels: Bi_4Br_4 crystal structure. The bc-plane displays 1D molecular chains along the *b*-axis. The ac-plane reveals AB stacking with b/2 interlayer translation and 180° rotation between adjacent layers. Chains are interconnected along *a*- and *c*-directions via van der Waals interactions. Within each chain, Bi atoms form a zigzag backbone via strong covalent bonding in a near-vertical configuration, while Br atoms terminate the outer Bi sites. (b) AFM topography of Bi_4Br_4 nanoribbons on WTe_2, showing aligned nanoribbons with regular shapes, flat surfaces, and sharp edges. Scale bar: 30 nm. (c) The height profile (red line in the inset) reveals a nanoribbon height distribution of 5–6 nm. Inset: larger-scale AFM image from (b); scale bar: 70 nm. (d–f) XPS characterization of the Bi_4Br_4/WTe_2 heterostructure. (d) Survey spectrum confirms no impurity elements. (e) Bi 4f and (f) Br 3d core-level spectra show characteristic valence states of Bi_4Br_4.

Raman and XRD further characterized the molecular vibrational modes and crystal structure of the heterostructure. The Raman spectrum (Figure 2a) displays distinct characteristic peaks at 81, 114, 134, 163, and 212 cm^{-1}, corresponding to the $^2A_1$, $^3A_1$, $^5A_1$, $^7A_1$, and $^9A_1$ modes of Td-WTe_2 [66]. However, the strong overlap of the WTe_2 peak at 114 cm^{-1} with the Bi_4Br_4 primary peak at 115 cm^{-1} [33] severely interferes with the clear detection of the film's Raman signal. Raman measurements on Bi_4Br_4 bulk crystals (Figure S4) reveal that the intrinsic peaks (115 cm^{-1} main peak, with two weak peaks at 102 and 125 cm^{-1}) are present only at a low laser power of 0.3 mW. Higher powers induce thermal damage, causing additional peaks or complete disappearance of the intrinsic signals, confirming the high thermal sensitivity of Bi_4Br_4. On the WTe_2 substrate, a clear Raman spectrum requires 2–3 mW—a power level that would thermally damage Bi_4Br_4 and eliminate its intrinsic signals. To avoid both peak overlap and thermal damage, the Bi_4Br_4 film grown on a silicon substrate was measured at 0.3 mW (Figure S5), showing a clear characteristic peak at 116 cm^{-1}.

Benefiting from the highly uniform in-plane orientation of the nanoribbons, we increased their areal density and grain size to enhance the XRD signal and applied a logarithmic scale (log scale) on the vertical axis to amplify weak signals, while simultaneously minimizing interference from the strong diffraction peaks of the substrate. As shown in Figure 2b, we observed diffraction peaks labeled in orange at $2\theta = 28°$, 37°, 48°, and 59°, which correspond to the (00l) family of planes of Bi_4Br_4 [19, 41]. Peaks originating from the WTe_2 substrate and the tantalum plate are labeled in black and gray, respectively.

To further confirm the crystal structure, STM images parallel to the nanoribbon long side reveal periodic lattice fringes (Figure S6g) with a 0.4 nm spacing, matching the *b*-axis constant (4.34 Å) of monoclinic Bi_4Br_4, confirming that the long side is the *b*-axis and consistent with Bi_4Br_4's anisotropic chain-like structure. The 0.6 nm fringe length is about half the *a*-axis constant (13.06 Å), and the lattice image matches the ab-plane atomic model (Figure S6h), verifying the Bi_4Br_4 lattice. The WTe_2 lattice fringe pattern (Figure S6a) shows ab-plane characterized by chain-like structures along the *a*-axis, with a 0.6 nm fringe spacing matching its *b*-axis constant (6.28 Å). This demonstrates that

the nanoribbon *b*-axis aligns with the WTe_2 *a*-axis—direct evidence for substrate-lattice-guided oriented growth. Figures S6b–S6d show nanoribbons with regular shapes, sharp edges, and flat surfaces, reflecting high crystalline quality. Thus, the STM results confirm the epitaxial relationship and demonstrate at the lattice scale that the nanoribbons are Bi_4Br_4, not other bismuth bromides.

Meanwhile, two annealing treatments reveal significant thermal instability of the Bi_4Br_4 nanoribbons: the elongated nanoribbons gradually shorten with annealing (Figures S6e–S6f), and their surfaces even exhibit segmentation, indicating signs of fracture (Figures S6i–S6k); a few have transformed into spherical and triangular Bi grains, as elevated temperatures induce thermal decomposition, consistent with our HRTEM observations (Figures S2–S3), high-temperature growth and annealing studies (Figures 3 and 4).

Further evidence for the formation of the heterostructure comes from EDS analysis. The EDS spectrum (Figure 2c) reveals a Bi:Br atomic ratio of 0.40:0.55 (approximately 1:1) and a W:Te ratio of 28.19:56.38 (1:2), both matching their expected stoichiometries and agreeing with the XPS quantitative analysis results in SI-Table 1. Other than C, O, and Al signals attributable to the environment and instrument, no impurity-related peaks are observed. The EDS elemental mapping in Figure 2d clearly reveals that Bi, Br, W, and Te are uniformly distributed on the heterostructure surface. These EDS results, together with the morphological, structural, and chemical characterization presented above, demonstrate the successful fabrication of the Bi_4Br_4/WTe_2 van der Waals heterostructure.

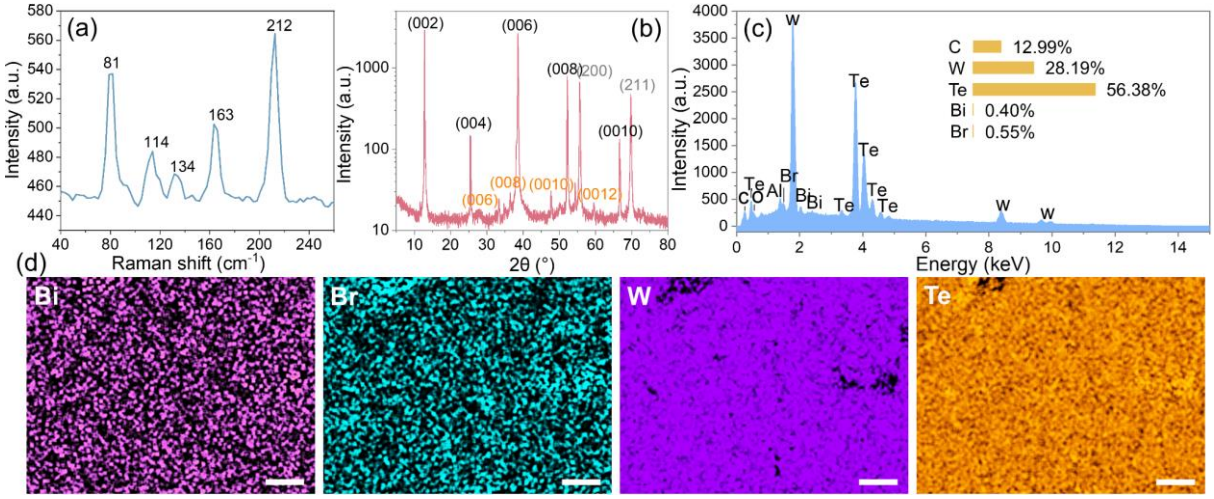

Figure 2. Characterization of the Bi_4Br_4/WTe_2 heterostructure. (a) Raman spectrum, (b) XRD pattern, (c) EDS spectrum, and (d) EDS elemental mapping, revealing the molecular structure, crystal lattice, and chemical composition of the heterostructure, respectively. (a) The Raman spectrum shows characteristic peaks of WTe_2. The WTe_2 peak at 114 cm^{-1} strongly overlaps with the main Raman peak of Bi_4Br_4 at 115 cm^{-1}, preventing clear identification of the film's signal. To avoid peak overlap, the film grown on Si substrate clearly displays the characteristic Raman peak of Bi_4Br_4 at 116 cm^{-1} (Figure S5). (b) XRD characterization of the Bi_4Br_4/WTe_2 heterostructure. A logarithmic vertical axis was used to amplify weak signals while minimizing interference from the strong substrate background. The diffraction peaks at $2\theta = 28°$, 37°, 48°, and 59° (labeled in orange) correspond to the (00l) family planes of Bi_4Br_4. Peaks originating from the WTe_2 substrate and the tantalum plate are labeled in black and gray, respectively. (c) The EDS spectrum confirms a Bi:Br atomic ratio of 0.40:0.55, which is approximately 1:1. The W:Te ratio is 28.19:56.38 (1:2). Both ratios are consistent with their expected stoichiometries. (d) EDS elemental mapping clearly reveals the uniform distribution of Bi, Br, W, and Te across the heterostructure surface. Scale bar: 200 μm.

We developed a two-step epitaxial growth method to synthesize Bi_4Br_4 nanoribbons on WTe_2 substrates. The process consists of depositing a Bi pre-layer, followed by the introduction of $BiBr_3$ vapor as a bromine source, enabling Bi_4Br_4 crystallization within an appropriate temperature window. The key to this method depends on precise substrate temperature control and independent rate monitoring to ensure an exact source ratio—both of which are essential for achieving high-quality morphology and crystallinity. We systematically investigated the influence of substrate temperature (100–160 °C) on structural evolution and overall film quality, examining its role during both the Bi pre-layer growth and bromination stages.

Given that Bi atomic chains form the backbone of Bi_4Br_4 nanoribbons, their grain size and density are closely correlated with the final size and distribution of the nanoribbons. To systematically investigate this relationship, we

varied the Bi-stage growth temperature (100, 130, and 160 ℃, Figures 3a–3c) while keeping the bromination temperature at a minimum to avoid interference.

In Figure 3a, the nanoribbons are densely distributed, with average dimensions of ~30 nm in length and ~15 nm in width. However, the low growth temperatures in both steps cause poor crystallization with amorphous regions (red circles), leading to rough surfaces and poor edge sharpness. At 130 ℃ (Figure 3b), the higher Bi-stage growth temperature improves Bi layer quality and bromination, driving grain coalescence and enhancing *b*-axis growth, increasing the length to 80–100 nm (max ~140 nm) without a notable change in width, albeit with a sparser spatial distribution, and the nanoribbons with regular shapes and sharp edges reflect improved crystallinity. Large-area 3D AFM topographic images are presented in Figures S7a–S7c. At 160 ℃ (Figure 3c), a further temperature increase reduces Bi density even more, severely hindering grain coalescence and growth. Consequently, short and sparse nanoribbons are observed, with the average length decreasing to ~40 nm. Since Bi deposition reduces while Br supply remains constant, the shortage of Bi reactant leads to excess Br, which forms a continuous amorphous coverage layer that is more visible on exposed substrate areas (red circles), compromising surface cleanliness. These results reveal a clear non-monotonic change in length: as the Bi-stage temperature increases, the nanoribbons first grow longer and then shorter, while their spatial density becomes progressively sparser with rising temperature.

This growth trend follows surface reaction kinetics. At low temperatures, low desorption increases Bi deposition and nucleation density. However, limited adatom mobility restricts surface diffusion, thereby hindering grain coalescence, ultimately producing small, dense grains. As the temperature rises, enhanced mobility promotes grain coalescence and longitudinal growth, significantly increasing nanoribbon length. Concurrently, higher desorption reduces the actual deposition amount, lowers nucleation density, and, together with grain coalescence, leads to a sparser distribution. At even higher temperatures, severe Bi desorption results in sparse nucleation and grain distribution that fails to coalesce, ultimately yielding short, sparsely distributed nanoribbons. Thus, the Bi-stage growth temperature significantly influences the final morphology of Bi_4Br_4 nanoribbons by regulating key processes like nucleation, desorption, migration, and grain coalescence.

After systematically investigating the effect of Bi temperature, we explored how bromination temperature affects the final morphology and surface quality. Appropriately increasing the bromination-stage temperature (130 ℃, Figures 3d–3f) leads to more complete surface reactions and better crystallinity, reducing amorphous regions and yielding large-area nanoribbons with regular shapes and sharp edges. More importantly, higher temperatures promote desorption of unreacted Br and improve overall surface cleanliness. Figures S7d–7f present the 3D topographic images of Figure 3e. Additional AFM images at smaller scan scales for finer surface and edge details under different growth temperatures are shown in Figure S8.

However, excessive temperatures (160 ℃, Figures 3g–3i) make Br readily desorb, hindering Bi_4Br_4 nanoribbon synthesis. Even when growth occurs, thermal disturbance can break their structure, causing fractures that shorten the nanoribbons and disrupt epitaxial alignment. Moreover, thermal decomposition breaks Bi–Br bonds, causing Br to volatilize and leading to a transition back to triangular Bi grains (yellow triangles). These observations reveal the significant thermal instability of the as-grown Bi_4Br_4 nanoribbons, as elevated temperature severely compromises the structural integrity of these 1D nanostructures. This conclusion is consistent with the annealing study in Figure 4, together with the HRTEM findings (Figures S2–S3) and the STM annealing results (Figures S6).

From Figure 3, the substrate temperature in both growth steps collectively determines the morphology (including crystal size, density and crystallinity), phase purity, and crystal orientation of the Bi_4Br_4 nanoribbons. Our experiments indicate that optimal film quality is achieved at well-matched intermediate temperatures: a Bi layer grown at 130 ℃ followed by bromination at 100–130 ℃. This combination provides good Bi layer quality and suitable bromination temperatures, which benefit reaction completeness and crystallinity. Lower or higher temperatures typically cause poor crystallization, incomplete reactions or structural degradation, ultimately impairing nanoribbon structural integrity and overall film quality.

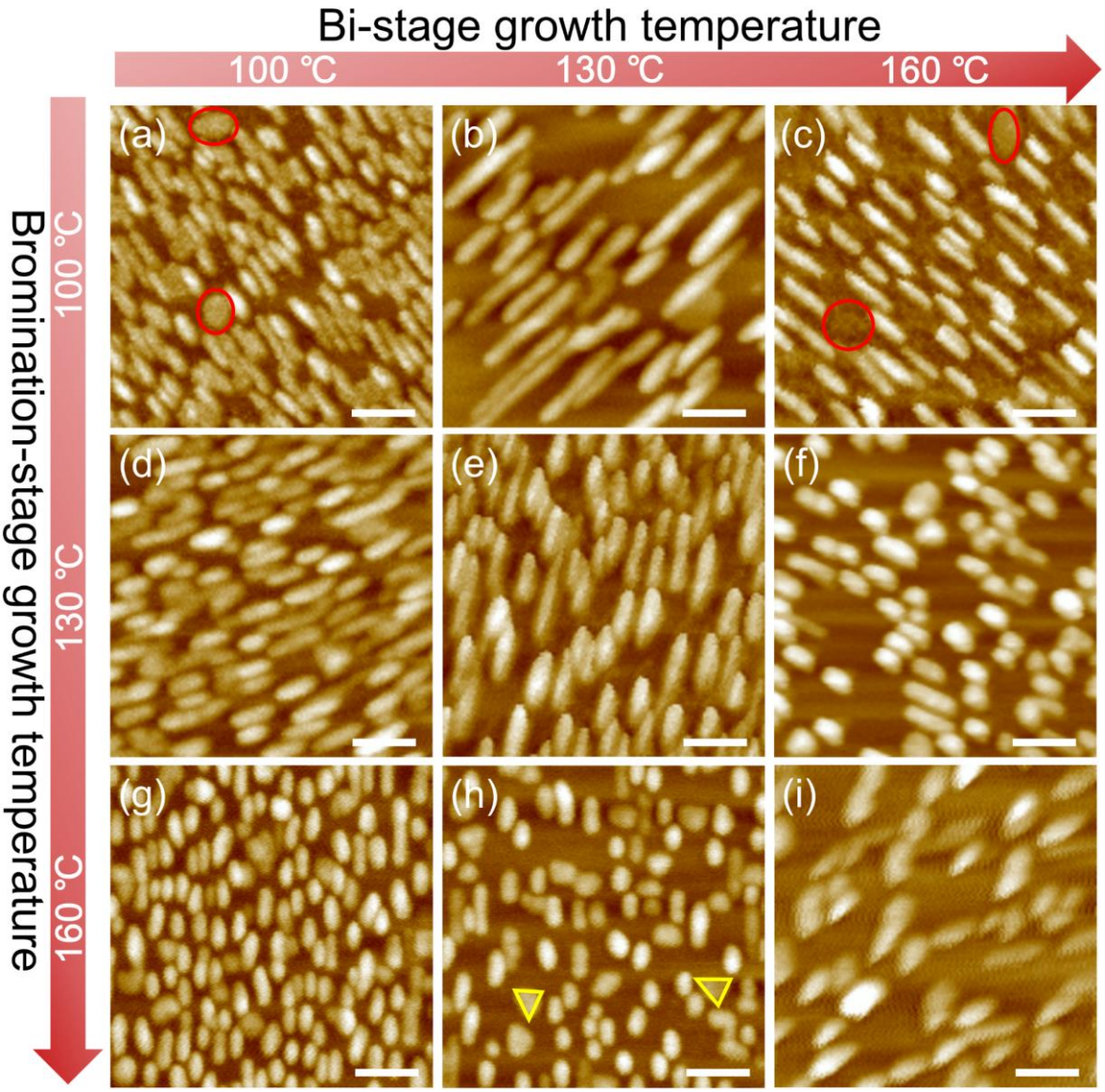

Figure 3. Temperature-dependent morphology of Bi_4Br_4 nanoribbons synthesized via a two-step growth method. The images show the effects of Bi-stage (horizontal: 100–160 °C) and bromination-stage (vertical: 100–160 °C) growth temperatures. (a) Low temperatures (100 °C in both steps) cause poor crystallization with amorphous regions (red circles), yielding short, densely distributed nanoribbons with rough surfaces and ill-defined edges. (b) Increasing Bi-stage temperature to 130 °C improves Bi quality and promotes bromination, yielding longer, better-shaped nanoribbons via grain coalescence, albeit with a sparser spatial distribution. (c) At 160 °C, a further Bi-stage temperature increase reduces Bi density even more, hindering grain coalescence, yielding shorter, sparser nanoribbons; excess Br forms a continuous amorphous coverage layer, reducing surface cleanliness. (d) Higher bromination temperature (130 °C) enhances surface reactions and crystallinity, reducing amorphous regions. (e) Good Bi layer quality and higher bromination temperature promote sufficient reaction, improved crystallinity, and regular nanoribbons with sharp edges. (f) Higher bromination temperature promotes desorption of excess Br and improves surface cleanliness. (g–i) Excessive bromination temperatures cause Br to desorb readily, hindering Bi_4Br_4 synthesis. Even when nanoribbons grow, thermal disturbance fractures them, shortening their length (g) and disrupting alignment (h, i). Thermal decomposition breaks Bi–Br bonds, forming triangular Bi grains (yellow triangles). Scale bar: 50 nm.

Following a systematic study of substrate temperature effects, we investigated the influence of the source deposition rate ratio on the epitaxial growth of Bi_4Br_4 on WTe_2. Here, the Bi deposition rate and substrate temperature were held constant, while the $BiBr_3$ deposition rate was varied to assess its impact on film quality. Our results establish the deposition rate ratio between Bi and $BiBr_3$ as another key parameter that critically controls the final film morphology and phase purity.

At an excessively low $BiBr_3$ deposition rate (0.6 ML min^{-1}, Figure 4a), the limited bromine supply in the reaction

environment and insufficient kinetic energy restrict effective interaction with the pre-deposited Bi layer, resulting in incomplete bromination and leaving triangular Bi grains on the surface. XPS semi-quantitative analysis (SI-Table 2) shows the Bi:Br atomic ratio of 30.92:6.13 (5:1), also indicating a large Bi excess. Within the optimal range of 1–1.2 ML min^{-1} (Figure 4b), the supply ratio of the two sources is balanced, promoting the formation of uniform, continuous Bi_4Br_4 nanoribbons with well-defined 1D morphology. Further increasing the $BiBr_3$ rate (1.5 ML min^{-1}, Figure 4c) leads to local accumulation of unreacted bromine source, forming rough amorphous regions that partially cover the nanoribbons and compromise their morphological integrity and phase purity. At 1.7 ML min^{-1} (Figure 4d), the surface is fully covered by a continuous amorphous overlayer, wherein aligned regular features along specific crystallographic directions remain discernible, accompanied by severe degradation in both edge sharpness and overall crystallinity.

Besides the source ratio, the annealing process is equally critical in determining the final film quality. In our two-step growth procedure, the annealing temperature is generally maintained at the growth temperature, with the duration scaled proportionally to the deposition time and limited to 30 minutes. However, excessively prolonged annealing is found to trigger significant thermal decomposition. As illustrated in Figure 4e, extending the annealing to 45 minutes leads to the decomposition of numerous Bi_4Br_4 nanoribbons, characterized by Bi–Br bond cleavage and Br volatilization, resulting in the formation of triangular metallic Bi grains on the substrate. With further extension to 1 hour (Figure 4f), the grain density decreases markedly, and the surface becomes nearly fully covered by triangular or spherical Bi particles, with no well-oriented Bi_4Br_4 nanostructures remaining. These observations clearly demonstrate the thermal instability of Bi_4Br_4 at elevated temperatures and highlight the importance of strictly controlled annealing duration for preserving its structural integrity.

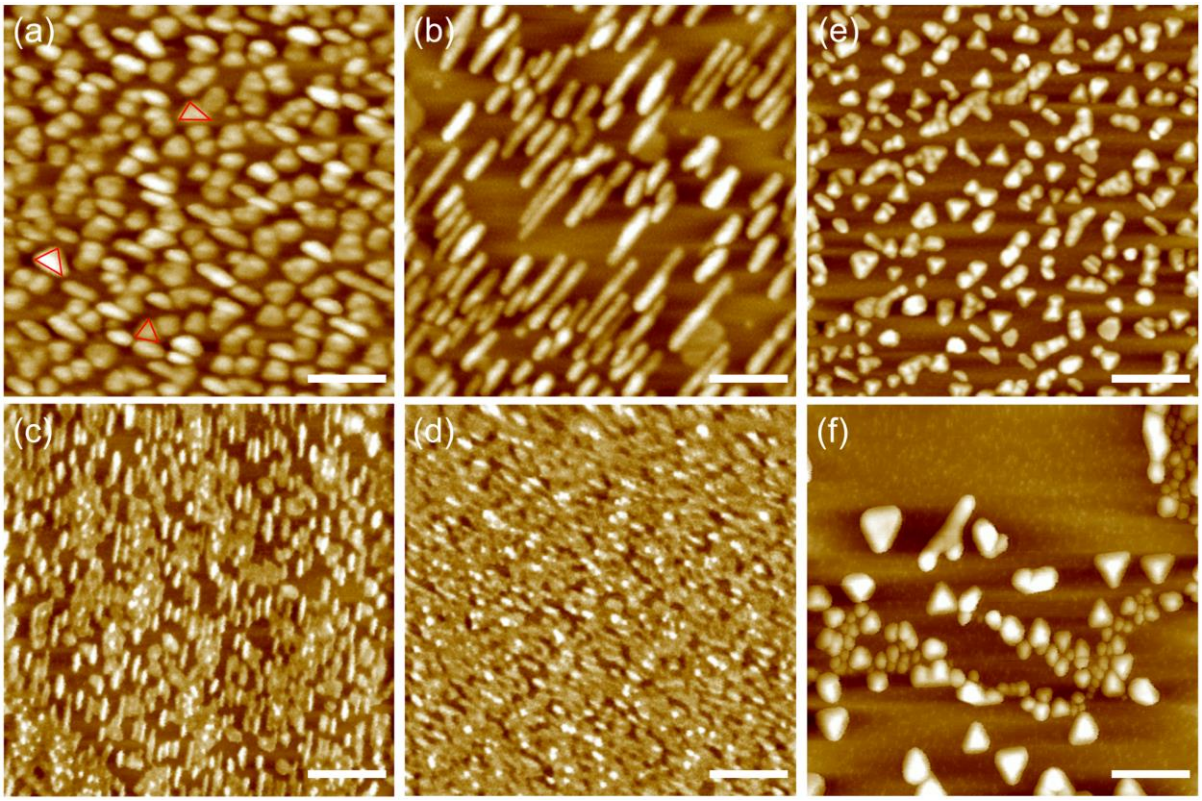

Figure 4. Influence of growth parameters on the morphology of Bi_4Br_4 nanostructures. (a–d) Effect of bromination rate: An optimal rate ensures complete reaction with Bi, while an excessive rate leads to surplus $BiBr_3$ on the substrate, degrading film quality. The red triangles in (a) mark metallic Bi grains. (e–f) Effect of prolonged annealing: Extended annealing decomposes the Bi_4Br_4 nanoribbons. This decomposition cleaves Bi–Br bonds and evaporates Br, converting the nanoribbons into triangular Bi grains and demonstrating the compound's thermal instability. Scale bar: 100 nm.

Based on the highly controllable two-step epitaxial growth method developed in this work, we have successfully synthesized thickness-tunable Bi_4Br_4 nanostructures on WTe_2 substrates. Theoretical calculations based on the crystal structure give an out-of-plane monolayer thickness of $10.03 \times \sin 107.4° \approx 0.96$ nm along the interlayer stacking direction, consistent with the reported value of ~0.98 nm for monolayer Bi_4Br_4 [25], thus providing a reliable basis

for thickness calibration. Through systematic optimization of growth temperature, source rate ratio, and annealing duration, we obtained large-area, uniform Bi_4Br_4 thin films (Figures 5a–d). By fine-tuning the deposition conditions, we fabricated nanostructures with two distinct thickness ranges: 2–4.5 nm (~2–5 layers) and 4.5–9 nm (~5–9 layers). We observed a positive correlation between increased nanoribbon thickness and both average lateral width (from ~15 nm to ~30 nm) and packing density. This yields more compact arrays, which are advantageous for integrated device fabrication. Furthermore, within localized regions of the same sample, Bi_4Br_4 nanoribbons with different layer numbers were found to coexist, offering a unique platform for systematic investigation of thickness-dependent topological properties within a single architecture.

Previous studies have reported the significant layer-number dependence of Bi_4Br_4's electronic structure [13, 27-29]. In the monolayer limit, it behaves as a 2D topological insulator with a nontrivial Z_2 invariant, hosting topologically protected 1D helical edge states. As thickness increases to the bulk limit, Bi_4Br_4 transitions into a higher-order topological insulator, where symmetry-protected bulk topology gives rise to hinge states. While thinner nanoribbons may contain monolayer regions, thus exhibiting the characteristics of a 2D topological insulator, thicker ones approach bulk electronic behavior. Our thickness-tunable nanoribbons therefore enable direct observation of the cross-dimensional evolution from 2D topological insulators to quasi-1D higher-order topological insulators within a single experiment. The layer-island growth mode of Bi_4Br_4 on WTe_2 (001) further leads to the natural formation of atomically sharp step edges on the (100) surface. These steps serve as ideal 1D boundaries for exploring topologically protected dissipationless edge transport. In multilayer regions, topological boundary states from different layers exhibit weak interlayer coupling, which becomes fully decoupled when the width exceeds ~5 nm [27], making them particularly suitable for constructing multi-channel, low-dissipation topological devices.

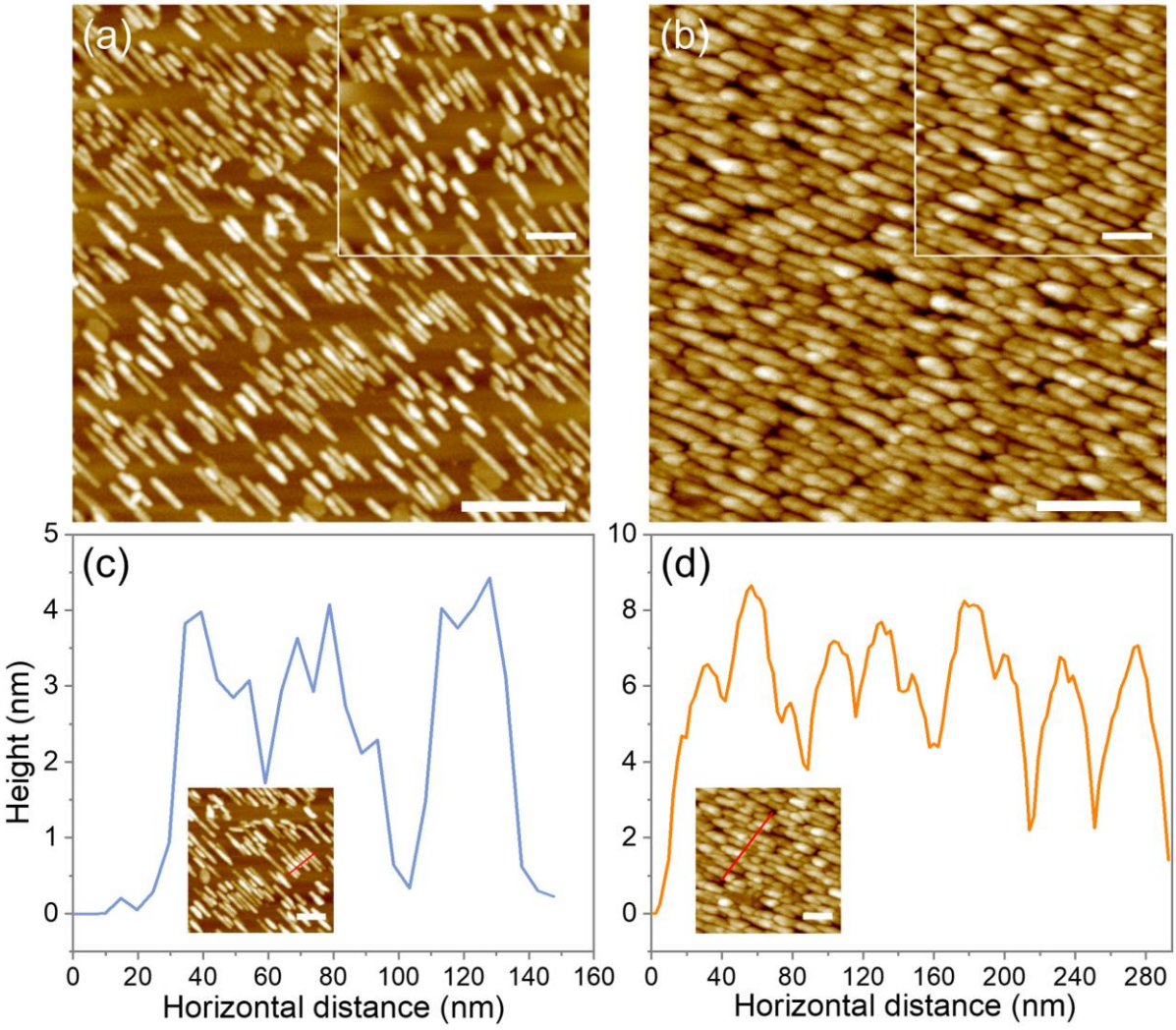

Figure 5. Evolution of Bi_4Br_4 nanoribbon morphology as a function of thickness. (a, b) AFM topography images reveal that higher thickness leads to larger width and a denser, more closely packed nanoribbon array. Figure S9 shows the 3D topography of the two insets, and Figure S10 shows larger-area AFM images corresponding to panel (b). Scale bars: 200 nm; insets: 100 nm. (c, d) The respective height maps for the structures in (a) and (b). The red

lines in the insets (Scale bars: 100 nm) denote the locations of the height profiles.

4 Conclusion

In summary, this work demonstrates that a two-step MBE approach using anisotropic WTe_2 substrates enables the controlled, oriented growth of Bi_4Br_4 nanoribbons—a 1D topological insulator. Through systematic optimization of key parameters including growth temperature, source rate ratio, and annealing conditions, we achieved precise control over nanoribbon morphology, phase purity, and thickness, thereby establishing the optimal window for high-quality epitaxial growth. The resulting nanoribbons exhibit macroscopic alignment, tunable thickness from 2 to 9 nm, and well-defined morphologies with sharp edges, overcoming the persistent challenges of random orientation and poor dimensional control in conventional methods. Furthermore, this system provides an ideal platform for investigating layer-dependent topological phase transitions within a single sample. The naturally formed atomically sharp step edges and weakly coupled multilayer configurations offer unique opportunities to explore dissipationless edge transport and multi-channel topological boundary states. Our study not only presents a general strategy for the oriented integration of 1D topological materials, but also paves the way for future research on topological transport, anisotropic optoelectronic responses, and quantum device engineering, thereby advancing topological insulators from fundamental research toward functional device applications.

Declaration of competing interest The authors declare no competing financial interest.

Data availability Data will be made available on request.

Electronic supplementary materials The online version contains supplementary material available at https://doi.org/10.15302/frontphys.2026.085208. Optical microscopy images of the sample and sample holder; Cross-sectional HRTEM characterization and its EDS elemental mapping of the heterostructure; XPS semi-quantitative analysis; Raman measurements of Bi_4Br_4 bulk single crystals; Raman spectrum of Bi_4Br_4 film grown on silicon substrate; STM characterization of the heterostructure; smaller-area AFM images under different growth temperatures; 3D AFM morphology data and larger-area AFM topography images for the Bi_4Br_4 oriented nanoribbons (DOC).

Acknowledgements This work was funded by the National Natural Science Foundation of China (Grant No. 62275061), Langyue Program (Grant No. LY2024-24), the Beijing National Laboratory for Condensed Matter Physics (Grant No. 2023BNLCMPKF007), and Technology Department of Guangdong Province (No. STKJ2024081).

References

1. M. Z. Hasan and C. L. Kane, Colloquium: Topological insulators, *Rev. Mod. Phys.* 82(4), 3045 (2010) https://doi.org/10.1103/RevModPhys.82.3045

2. X. L. Qi and S. C. Zhang, Topological insulators and superconductors, *Rev. Mod. Phys.* 83(4), 1057 (2011) https://doi.org/10.1103/RevModPhys.83.1057

3. P. Liu, J. R. Williams, and J. J. Cha, Topological nanomaterials, *Nat. Rev. Mater.* 4(7), 479 (2019) https://doi.org/10.1038/s41578-019-0113-4

4. B. J. Wieder, B. Bradlyn, J. Cano, Z. Wang, M. G. Vergniory, L. Elcoro, A. A. Soluyanov, C. Felser, T. Neupert, N. Regnault, and B. A. Bernevig, Topological materials discovery from crystal symmetry, *Nat. Rev. Mater.* 7(3), 196 (2021) https://doi.org/10.1038/s41578-021-00380-2

5. L. Fu and C. L. Kane, Topological insulators with inversion symmetry, *Phys. Rev. B* 76(4), 045302 (2007) https://doi.org/10.1103/PhysRevB.76.045302

6. Y. Tokura, K. Yasuda, and A. Tsukazaki, Magnetic topological insulators, *Nat. Rev. Phys.* 1(2), 126 (2019) https://doi.org/10.1038/s42254-018-0011-5

7. M. J. Gilbert, Topological electronics, *Commun. Phys.* 4(1), 70 (2021) https://doi.org/10.1038/s42005-021-00569-5

8. Y. Wang and H. Yang, Spin–orbit torques based on topological materials, *Acc. Mater. Res.* 3(10), 1061 (2022) https://doi.org/10.1021/accountsmr.2c00123

9. G. Zhang, H. Wu, L. Zhang, L. Yang, Y. Xie, F. Guo, H. Li, B. Tao, G. Wang, W. Zhang, and H. Chang, Two-dimensional van der Waals topological materials: Preparation, properties, and device applications, *Small* 18(47), 2204380 (2022) https://doi.org/10.1002/smll.202204380

10. P. Li, X. Yang, Q. S. Jiang, Y. Z. Wu, and W. Xun, Built-in electric field and strain tunable valley-related multiple topological phase transitions in $VSiXN_4$ (X = C, Si, Ge, Sn, Pb) monolayers, *Phys. Rev. Mater.* 7(6), 064002 (2023) https://doi.org/10.1103/PhysRevMaterials.7.064002

11. W. Xun, X. Liu, Y. Zhang, Y. Z. Wu, and P. Li, Stacking-, strain-engineering induced altermagnetism, multipiezo effect, and topological state in two-dimensional materials, *Appl. Phys. Lett.* 126(16), 161903 (2025) https://doi.org/10.1063/5.0267525

12. C. Yoon, C.C. Liu, H. Min, and F. Zhang, Quasi-one-dimensional higher-order topological insulators, arXiv: 2005.14710 (2005)

13. J. Han, W. Xiao, and Y. Yao, Quasi-one-dimensional topological material Bi_4X_4(X=Br,I), *Adv. Phys. X* 7(1), 2057234 (2022) https://doi.org/10.1080/23746149.2022.2057234

14. J. Zhong, M. Yang, W. Zhao, K. Zhai, X. Zhen, L. Zhang, D. Mu, Y. Liu, Z. Shi, N. Cheng, W. Zhou, J. Wang, W. Hao, Z. Hu, J. Zhuang, J. Lü, and Y. Du, Coalescence of multiple topological orders in quasi-one-dimensional bismuth halide chains, *Nat. Commun.* 16(1), 1163 (2025) https://doi.org/10.1038/s41467-025-56593-4

15. G. Autès, A. Isaeva, L. Moreschini, J. C. Johannsen, A. Pisoni, R. Mori, W. Zhang, T. G. Filatova, A. N. Kuznetsov, L. Forró, W. Van den Broek, Y. Kim, K. S. Kim, A. Lanzara, J. D. Denlinger, E. Rotenberg, A. Bostwick, M. Grioni, and O. V. Yazyev, A novel quasi-one-dimensional topological insulator in bismuth iodide β-Bi_4I_4, *Nat. Mater.* 15(2), 154 (2016) https://doi.org/10.1038/nmat4488

16. R. Noguchi, M. Kobayashi, K. Kawaguchi, W. Yamamori, K. Aido, C. Lin, H. Tanaka, K. Kuroda, A. Harasawa, V. Kandyba, M. Cattelan, A. Barinov, M. Hashimoto, D. Lu, M. Ochi, T. Sasagawa, and T. Kondo, Robust weak topological insulator in the bismuth halide $Bi_4Br_2I_2$, *Phys. Rev. Lett.* 133(8), 086602 (2024) https://doi.org/10.1103/PhysRevLett.133.086602

17. J. Zhong, J. Wang, M. Yang, J. Liu, Z. Ren, A. Huang, Z. Shi, Z. Zhu, Y. Shi, W. Hao, J. Zhuang, and Y. Du, Field manipulation of Weyl modes in an ideal Dirac semimetal, *Nat. Commun.* 16(1), 10785 (2025) https://doi.org/10.1038/s41467-025-65832-7

18. Y. Qi, W. Shi, P. Werner, P. G. Naumov, W. Schnelle, L. Wang, K. G. Rana, S. Parkin, S. A. Medvedev, B. Yan, and C. Felser, Pressure-induced superconductivity and topological quantum phase transitions in a quasi-one-dimensional topological insulator: Bi_4I_4, *npj Quantum Mater.* 3, 4 (2018) https://doi.org/10.1038/s41535-018-0078-3

19. X. Li, D. Chen, M. Jin, D. Ma, Y. Ge, J. Sun, W. Guo, H. Sun, J. Han, W. Xiao, J. Duan, Q. Wang, C. C. Liu, R. Zou, J. Cheng, C. Jin, J. Zhou, J. B. Goodenough, J. Zhu, and Y. Yao, Pressure-induced phase transitions and superconductivity in a quasi-1-dimensional topological crystalline insulator α-Bi_4Br_4, *Proc. Natl. Acad. Sci. USA* 116(36), 17696 (2019) https://doi.org/10.1073/pnas.1909276116

20. W. Liu, X. Xiong, M. Liu, X. Xing, H. Chen, H. Ye, J. Han, and Z. Wei, Bi_4Br_4-based saturable absorber with robustness at high power for ultrafast photonic device, *Appl. Phys. Lett.* 120(5), 053108 (2022) https://doi.org/10.1063/5.0077148

21. Y. Liu, R. Chen, Z. Zhang, M. Bockrath, C. N. Lau, Y. F. Zhou, C. Yoon, S. Li, X. Liu, N. Dhale, B. Lv, F. Zhang, K. Watanabe, T. Taniguchi, J. Huang, M. Yi, J. S. Oh, and R. J. Birgeneau, Gate-tunable transport in quasi-one-dimensional α-Bi_4I_4 field effect transistors, *Nano Lett.* 22(3), 1151 (2022) https://doi.org/10.1021/acs.nanolett.1c04264

22. J. Han, P. Mao, H. Chen, J. X. Yin, M. Wang, D. Chen, Y. Li, J. Zheng, X. Zhang, D. Ma, Q. Ma, Z. M. Yu, J. Zhou, C. C. Liu, Y. Wang, S. Jia, Y. Weng, M. Z. Hasan, W. Xiao, and Y. Yao, Optical bulk-boundary dichotomy in a quantum spin Hall insulator, *Sci. Bull. (Beijing)* 68(4), 417 (2023) https://doi.org/10.1016/j.scib.2023.01.038

23. J. J. Zhou, W. Feng, C. C. Liu, S. Guan, and Y. Yao, Large-gap quantum spin Hall insulator in single layer bismuth monobromide Bi_4Br_4, *Nano Lett.* 14(8), 4767 (2014) https://doi.org/10.1021/nl501907g

24. X. Peng, X. Zhang, X. Dong, D. Ma, D. Chen, Y. Li, J. Li, J. Han, Z. Wang, C. C. Liu, J. Zhou, W. Xiao, and Y. Yao, Observation of topological edge states on α-Bi_4Br_4 nanowires grown on $TiSe_2$ substrates, *J. Phys. Chem. Lett.* 12(43), 10465 (2021) https://doi.org/10.1021/acs.jpclett.1c02586

25. M. Yang, Y. Liu, W. Zhou, C. Liu, D. Mu, Y. Liu, J. Wang, W. Hao, J. Li, J. Zhong, Y. Du, and J. Zhuang, Large-gap quantum spin Hall state and temperature-induced Lifshitz transition in Bi_4Br_4, *ACS Nano* 16(2), 3036 (2022) https://doi.org/10.1021/acsnano.1c10539

26. J. K. Hofmann, H. Jeon, S. M. Hus, Y. Zhang, M. Zheng, T. Wichmann, A. P. Li, J. J. Zhou, Z. Wang, Y. Yao, B. Voigtländer, F. S. Tautz, and F. Lüpke, Shear-resistant topology in the quasi-one-dimensional van der Waals material Bi_4Br_4, *Phys. Rev. B* 111(24), 245415 (2025) https://doi.org/10.1103/tdp5-wmqc

27. J. J. Zhou, W. Feng, G. B. Liu, and Y. Yao, Topological edge states in single- and multi-layer Bi_4Br_4, *New J. Phys.* 17(1), 015004 (2015) https://doi.org/10.1088/1367-2630/17/1/015004

28. Y. T. Yao, X. Zhou, Y. C. Hung, H. Lin, A. Bansil, and T. R. Chang, Feature-energy duality of topological boundary states in a multilayer quantum spin Hall insulator, *Phys. Rev. B* 109(15), 155143 (2024) https://doi.org/10.1103/PhysRevB.109.155143

29. R. Noguchi, M. Kobayashi, Z. Jiang, K. Kuroda, T. Takahashi, Z. Xu, D. Lee, M. Hirayama, M. Ochi, T. Shirasawa, P. Zhang, C. Lin, C. Bareille, S. Sakuragi, H. Tanaka, S. Kunisada, K. Kurokawa, K. Yaji, A. Harasawa, V. Kandyba, A. Giampietri, A. Barinov, T. K. Kim, C. Cacho, M. Hashimoto, D. Lu, S. Shin, R. Arita, K. Lai, T. Sasagawa, and T. Kondo, Evidence for a higher-order topological insulator in a three-dimensional material built from van der Waals stacking of bismuth-halide chains, *Nat. Mater.* 20(4), 473 (2021) https://doi.org/10.1038/s41563-020-00871-7

30. J. Huang, S. Li, C. Yoon, J. S. Oh, H. Wu, X. Liu, N. Dhale, Y. F. Zhou, Y. Guo, Y. Zhang, M. Hashimoto, D. Lu, J. Denlinger, X. Wang, C. N. Lau, R. J. Birgeneau, F. Zhang, B. Lv, and M. Yi, Room-temperature topological phase transition in quasi-one-dimensional material Bi_4I_4, *Phys. Rev. X* 11(3), 031042 (2021) https://doi.org/10.1103/PhysRevX.11.031042

31. N. Shumiya, M. S. Hossain, J. X. Yin, Z. Wang, M. Litskevich, C. Yoon, Y. Li, Y. Yang, Y. X. Jiang, G. Cheng, Y. C. Lin, Q. Zhang, Z. J. Cheng, T. A. Cochran, D. Multer, X. P. Yang, B. Casas, T. R. Chang, T. Neupert, Z. Yuan, S. Jia, H. Lin, N. Yao, L. Balicas, F. Zhang, Y. Yao, and M. Z. Hasan, Evidence of a room-temperature quantum spin Hall edge state in a higher-order topological insulator, *Nat. Mater.* 21(10), 1111 (2022) https://doi.org/10.1038/s41563-022-01304-3

32. W. Zhao, M. Yang, R. Xu, X. Du, Y. Li, K. Zhai, C. Peng, D. Pei, H. Gao, Y. Li, L. Xu, J. Han, Y. Huang, Z. Liu, Y. Yao, J. Zhuang, Y. Du, J. Zhou, Y. Chen, and L. Yang, Topological electronic structure and spin texture of quasi-one-dimensional higher-order topological insulator Bi_4Br_4, *Nat. Commun.* 14(1), 8089 (2023) https://doi.org/10.1038/s41467-023-43882-z

33. M. S. Hossain, Q. Zhang, Z. Wang, N. Dhale, W. Liu, M. Litskevich, B. Casas, N. Shumiya, J. X. Yin, T. A. Cochran, Y. Li, Y. X. Jiang, Y. Zhang, G. Cheng, Z. J. Cheng, X. P. Yang, N. Yao, T. Neupert, L. Balicas, Y. Yao, B. Lv, and M. Z. Hasan, Quantum transport response of topological hinge modes, *Nat. Phys.* 20(5), 776 (2024) https://doi.org/10.1038/s41567-024-02388-1

34. K. S. Lin, G. Palumbo, Z. Guo, Y. Hwang, J. Blackburn, D. P. Shoemaker, F. Mahmood, Z. Wang, G. A. Fiete, B. J. Wieder, and B. Bradlyn, Spin-resolved topology and partial axion angles in three-dimensional insulators, *Nat. Commun.* 15(1), 550 (2024) https://doi.org/10.1038/s41467-024-44762-w

35. C. C. Liu, J. J. Zhou, Y. Yao, and F. Zhang, Weak topological insulators and composite Weyl semimetals: β-Bi_4X_4 (X=Br, I), *Phys. Rev. Lett.* 116(6), 066801 (2016) https://doi.org/10.1103/PhysRevLett.116.066801

36. R. Noguchi, T. Takahashi, K. Kuroda, M. Ochi, T. Shirasawa, M. Sakano, C. Bareille, M. Nakayama, M. D. Watson, K. Yaji, A. Harasawa, H. Iwasawa, P. Dudin, T. K. Kim, M. Hoesch, V. Kandyba, A. Giampietri, A. Barinov, S. Shin, R. Arita, T. Sasagawa, and T. Kondo, A weak topological insulator state in quasi-one-dimensional bismuth iodide, *Nature* 566(7745), 518 (2019) https://doi.org/10.1038/s41586-019-0927-7

37. J. S. Oh, T. Xu, N. Dhale, S. Li, C. Lei, C. Yoon, W. Liu, J. Huang, H. Wu, M. Hashimoto, D. Lu, C. Jozwiak, A. Bostwick, E. Rotenberg, C. N. Lau, B. Lv, F. Zhang, R. J. Birgeneau, and M. Yi, Ideal weak topological insulator and protected helical saddle points, *Phys. Rev. B* 108(20), L201104 (2023) https://doi.org/10.1103/PhysRevB.108.L201104

38. W. X. Zhao, M. Yang, X. Du, Y. D. Li, K. Y. Zhai, Y. Q. Hu, J. F. Han, Y. Huang, Z. K. Liu, Y. G. Yao, J. C. Zhuang, Y. Du, J. J. Zhou, Y. L. Chen, and L. X. Yang, Topological phase transition in quasi-one-dimensional bismuth iodide Bi_4I_4, *npj Quantum Mater.* 9, 103 (2024) https://doi.org/10.1038/s41535-024-00711-w

39. D. Y. Chen, D. S. Ma, Y. Li, Z. Z. Du, X. Xiong, Y. He, J. Duan, J. Han, D. Chen, W. Xiao, and Y. Yao, Quantum transport properties in single crystals of α-Bi_4I_4, *Phys. Rev. Mater.* 2(11), 114408 (2018) https://doi.org/10.1103/PhysRevMaterials.2.114408

40. P. Wang, F. Tang, P. Wang, H. Zhu, C. W. Cho, J. Wang, X. Du, Y. Shao, and L. Zhang, Quantum transport properties of β-Bi_4I_4 near and well beyond the extreme quantum limit, *Phys. Rev. B* 103(15), 155201 (2021) https://doi.org/10.1103/PhysRevB.103.155201

41. D. Y. Chen, D. Ma, J. Duan, D. Chen, H. Liu, J. Han, and Y. Yao, Quantum transport evidence of boundary states and Lifshitz transition in Bi_4Br_4, *Phys. Rev. B* 106(7), 075206 (2022) https://doi.org/10.1103/PhysRevB.106.075206

42. M. Yang, W. Zhao, D. Mu, Z. Shi, J. Zhong, Y. Li, Y. Liu, J. Zhong, N. Cheng, W. Zhou, J. Wang, Y. Shi, Y. Sun, W. Hao, L. Yang, J. Zhuang, and Y. Du, Mass acquisition of Dirac fermions in Bi_4I_4 by spontaneous symmetry breaking, *Phys. Rev. Lett.* 133(25), 256601 (2024) https://doi.org/10.1103/PhysRevLett.133.256601

43. J. Lefeuvre, M. Kobayashi, G. Patriarche, N. Findling, D. Troadec, M. Ferrier, S. Guéron, H. Bouchiat, T. Sasagawa, and R. Deblock, Quantum coherent transport of 1D ballistic states in second-order topological insulator Bi_4Br_4, *Phys. Rev. X* 16(1), 011031 (2026) https://doi.org/10.1103/2bqq-t7ml

44. C. D. Hinostroza, L. Rodrigues de Faria, G. H. Cassemiro, J. Larrea Jiménez, A. Jefferson da Silva Machado, W. H. Brito, and V. Martelli, Structural investigation of the quasi-one-dimensional topological insulator Bi_4I_4, *Phys. Rev. B* 109(17), 174105 (2024) https://doi.org/10.1103/PhysRevB.109.174105

45. S. J. Allison, D. L. M. Cordova, M. Hasib, T. Aoki, and M. Q. Arguilla, Nanoparticle-directed bimodal crystallization of the quasi-1D van der Waals phase, Bi_4I_4, *Chem. Sci. (Camb.)* 15(13), 4811 (2024) https://doi.org/10.1039/D3SC06456E

46. S. Yu, J. Deng, W. Liu, Y. Zhang, Y. Sun, N. Dhale, S. Li, W. Ma, Z. Wang, P. Wu, Z. Liang, X. Zhang, B. Lv, Z. Wang, Z. Wang, and X. Chen, Observation of Robust One-Dimensional Edge Channels in a Three-Dimensional Quantum Spin Hall Insulator, *Phys. Rev. X* 14(4), 041048 (2024) https://doi.org/10.1103/PhysRevX.14.041048

47. M. N. Khan and M. Alam, Dissipationless edge transport in single-layer topological insulator Bi_4Br_4 based device under high vacancy concentration, *J. Phys.: Condens. Matter* 37(19), 195501 (2025) https://doi.org/10.1088/1361-648X/adc5cf

48. J. Zhong, M. Yang, J. Wang, Y. Li, C. Liu, D. Mu, Y. Liu, N. Cheng, Z. Shi, L. Yang, J. Zhuang, Y. Du, and W. Hao, Observation of anomalous planar Hall effect induced by one-dimensional weak antilocalization, *ACS Nano* 18(5), 4343 (2024) https://doi.org/10.1021/acsnano.3c10120

49. P. Wang, G. Yu, Y. H. Kwan, Y. Jia, S. Lei, S. Klemenz, F. A. Cevallos, R. Singha, T. Devakul, K. Watanabe, T. Taniguchi, S. L. Sondhi, R. J. Cava, L. M. Schoop, S. A. Parameswaran, and S. Wu, One-dimensional Luttinger liquids in a two-dimensional moiré lattice, *Nature* 605(7908), 57 (2022) https://doi.org/10.1038/s41586-022-04514-6

50. H. Li, Z. Xiang, T. Wang, M. H. Naik, W. Kim, J. Nie, S. Li, Z. Ge, Z. He, Y. Ou, R. Banerjee, T. Taniguchi, K. Watanabe, S. Tongay, A. Zettl, S. G. Louie, M. P. Zaletel, M. F. Crommie, and F. Wang, Imaging tunable Luttinger liquid systems in van der Waals heterostructures, *Nature* 631(8022), 765 (2024) https://doi.org/10.1038/s41586-024-07596-6

51. S. Xu, X. Meng, X. Zhang, C. Zhang, J. Bai, Y. Jiang, X. Li, C. Wang, P. Mao, J. Han, and Y. Yao, Molecular beam epitaxy growth of topological insulator Bi_4Br_4 on silicon for the infrared applications, *Quantum Front.* 3(1), 16 (2024) https://doi.org/10.1007/s44214-024-00062-4

52. X. Zhang, X. Xing, J. Li, X. Peng, L. Qiao, Y. Liu, X. Xiong, J. Han, W. Liu, W. Xiao, and Y. Yao, Controllable epitaxy of quasi-one-dimensional topological insulator α-Bi_4Br_4 for the application of saturable absorber, *Appl. Phys. Lett.* 120(9), 093103 (2022) https://doi.org/10.1063/5.0083807

53. S. Xu, Y. Li, X. Zhang, C. Zhang, Y. Dong, J. Bai, H. Gao, N. Cheng, C. Zhao, L. Zhao, and J. Han, Molecular beam epitaxy of quasi-1D α-Bi_4Br_4 nanoribbon/$NbSe_2$ heterostructures, *Mater. Today Phys.* 58, 101842 (2025) https://doi.org/10.1016/j.mtphys.2025.101842

54. T. Iizuka, H. Yuan, Y. Mita, A. Higo, S. Yasunaga, and M. Ezawa, Experimental demonstration of position-controllable topological interface states in high-frequency Kitaev topological integrated circuits, *Commun. Phys.* 6(1), 279 (2023) https://doi.org/10.1038/s42005-023-01404-9

55. H. J. Han, S. Kumar, G. Jin, X. Ji, J. L. Hart, D. J. Hynek, Q. P. Sam, V. Hasse, C. Felser, D. G. Cahill, R. Sundararaman, and J. J. Cha, Topological metal MoP nanowire for interconnect, *Adv. Mater.* 35(13), 2208965 (2023) https://doi.org/10.1002/adma.202208965

56. K. Flensberg, F. von Oppen, and A. Stern, Engineered platforms for topological superconductivity and Majorana zero modes, *Nat. Rev. Mater.* 6(10), 944 (2021) https://doi.org/10.1038/s41578-021-00336-6

57. J. Qi, C. Z. Chen, J. Song, J. Liu, K. He, Q. F. Sun, and X. C. Xie, Edge supercurrent in Josephson junctions based on topological materials, *Sci. China Phys. Mech. Astron.* 68(2), 227401 (2025) https://doi.org/10.1007/s11433-024-2520-9

58. T. Hirahara, G. Bihlmayer, Y. Sakamoto, M. Yamada, H. Miyazaki, S. i. Kimura, S. Blügel, and S. Hasegawa, Interfacing 2D and 3D Topological Insulators: Bi(111) Bilayer on Bi_2Te_3, *Phys. Rev. Lett.* 107(16), 166801 (2011) https://doi.org/10.1103/PhysRevLett.107.166801

59. J. Zhuang, J. Li, Y. Liu, D. Mu, M. Yang, Y. Liu, W. Zhou, W. Hao, J. Zhong, and Y. Du, Epitaxial growth of quasi-one-dimensional bismuth-halide chains with atomically sharp topological non-trivial edge states, *ACS Nano* 15, 14850 (2021) https://doi.org/10.1021/acsnano.1c04928

60. B. Rahman Rano, I. M. Syed, and S. H. Naqib, Elastic, electronic, bonding, and optical properties of WTe_2 Weyl semimetal: A comparative investigation with $MoTe_2$ from first principles, *Results Phys.* 19, 103639 (2020) https://doi.org/10.1016/j.rinp.2020.103639

61. J. M. Woods, D. Hynek, P. Liu, M. Li, and J. J. Cha, Synthesis of WTe_2 nanowires with increased electron scattering, *ACS Nano* 13(6), 6455 (2019) https://doi.org/10.1021/acsnano.8b09342

62. M. N. Ali, J. Xiong, S. Flynn, J. Tao, Q. D. Gibson, L. M. Schoop, T. Liang, N. Haldolaarachchige, M. Hirschberger, N. P. Ong, and R. J. Cava, Large, non-saturating magnetoresistance in WTe_2, *Nature* 514(7521), 205 (2014) https://doi.org/10.1038/nature13763

63. P. Li, Y. Wen, X. He, Q. Zhang, C. Xia, Z. M. Yu, S. A. Yang, Z. Zhu, H. N. Alshareef, and X. X. Zhang, Evidence for topological type-II Weyl semimetal WTe_2, *Nat. Commun.* 8(1), 2150 (2017) https://doi.org/10.1038/s41467-017-02237-1

64. X. Jiang, T. Yilmaz, E. Vescovo, and D. Lu, Manipulating topological properties in Bi_2Se_3/BiSe/transition metal dichalcogenide heterostructures with interface charge transfer, *Phys. Rev. B* 109(11), 115112 (2024) https://doi.org/10.1103/PhysRevB.109.115112

65. Z. Zhao, Y. Lin, and A. Avsar, Novel spintronic effects in two-dimensional van der Waals heterostructures, *npj 2D Mater. Appl.* 9(1), 30 (2025) https://doi.org/10.1038/s41699-025-00546-4

66. X. Ma, P. Guo, C. Yi, Q. Yu, A. Zhang, J. Ji, Y. Tian, F. Jin, Y. Wang, K. Liu, T. Xia, Y. Shi, and Q. Zhang, Raman scattering in the transition-metal dichalcogenides of 1T′-$MoTe_2$, T_d-$MoTe_2$, and T_d-WTe_2, *Phys. Rev. B* 94(21), 214105 (2016) https://doi.org/10.1103/PhysRevB.94.214105